

Qingxi Meng · Ming Li · Jinsheng Zhang

Density functional computations of enantioselective alkynylation of aldehyde catalyzed by chiral zinc(II)-complexes

Received: 5 May 2005 / Accepted: 23 November 2005 / Published online: 14 January 2006
© Springer-Verlag 2006

Abstract The enantioselective alkynylation of aldehyde catalyzed by chiral zinc(II)-complexes was studied by means of the density functional theory (DFT). All the structures were optimized completely at the B3LYP/6-31G (d,p) level. To obtain more exact energies, single-point energy calculations at B3LYP/6-31+G(d,p) level were carried out on the B3LYP/6-31G(d,p) geometries. As shown, this enantioselective alkynylation was endothermic. The chirality-determining step for the alkynylation was the formation of the catalyst–ethanol complexes and the transition states for this step involved a six-membered ring. The dominant products predicted theoretically were of (*R*)-chirality, in good agreement with experiment.

Keywords Enantioselective alkynylation · Chiral zinc(II)-catalyzed complexes · DFT · Reaction mechanism

Introduction

The enantioselective formation of the C–C bonds has attracted much attention [1–19]. The enantioselective addition of terminal alkynes to aldehydes [7–18] or ketones [19] directly affords optically active propargyl alcohols that are useful and versatile building blocks that enjoy wide application in chemical synthesis. Chiral zinc(II) complexes are the active catalysts used to induce high stereoselectivity for these reactions [7–19].

Noyori's research group [20, 21] put forward a double-zinc model of the reaction mechanism of the enantioselective addition of ZnR_2 to aldehydes and studied the mechanism by quantum chemical methods [22, 23]. Gong's group [24] studied the asymmetric alkynylation of C=O and C=N bonds catalyzed by double-zinc complexes both experimentally and theoretically. Single-zinc complexes have been found experimentally [20, 21, 25]. Carreira's group investigated the enantioselective addition of terminal alkynes to aldehydes and suggested a single-zinc model of the reaction mechanism [2, 8–15]. However, the theoretical data available for the mechanism of the enantioselective addition of terminal alkynes to aldehydes are rather limited [22, 23] and quantum chemical studies on the mechanism of the single-zinc-catalyzed enantioselective alkynylation are rare. Therefore, in order to understand the mechanism of the single-zinc-catalyzed enantioselective alkynylation in detail, the chiral zinc(II)-catalyzed enantioselective alkynylation of aldehydes has been studied in the present work.

Models and computations

The present studies are based on the chiral zinc(II)-catalyzed enantioselective alkynylation of aldehyde [8–15]. As showed in Fig. 1, the attack of aldehyde on the intermediate states 6M and 6M' leads to four plausible reaction paths. In the following discussion, the attack of aldehyde on 6M and 6M' from the *re*-surface is marked by "a" and that from the *si*-surface by "b".

All intermediates and transition states are fully optimized using density-functional theory (DFT) at the B3LYP/6-31G (d,p) level. Vibrational and natural bond orbital (NBO) analyses were performed at the same computational level. All transition states were optimized until their Hessian matrices had a sole imaginary eigenvalue and were verified by internal reaction coordinate (IRC) calculations at the B3LYP/6-31G(d,p) level and by animating the negative eigenvector coordinates with the visualization program (Molekel 4.3) [26, 27]. The IRC calculations for some transition states are

Q. Meng · M. Li (✉) · J. Zhang
Department of Chemistry, Southwest-China Normal University,
Chongqing 400715, People's Republic of China
e-mail: liming@swnu.edu.cn

Q. Meng
Department of Chemistry and Material Science,
Shandong Agricultural University,
Taian, Shandong 271018, People's Republic of China

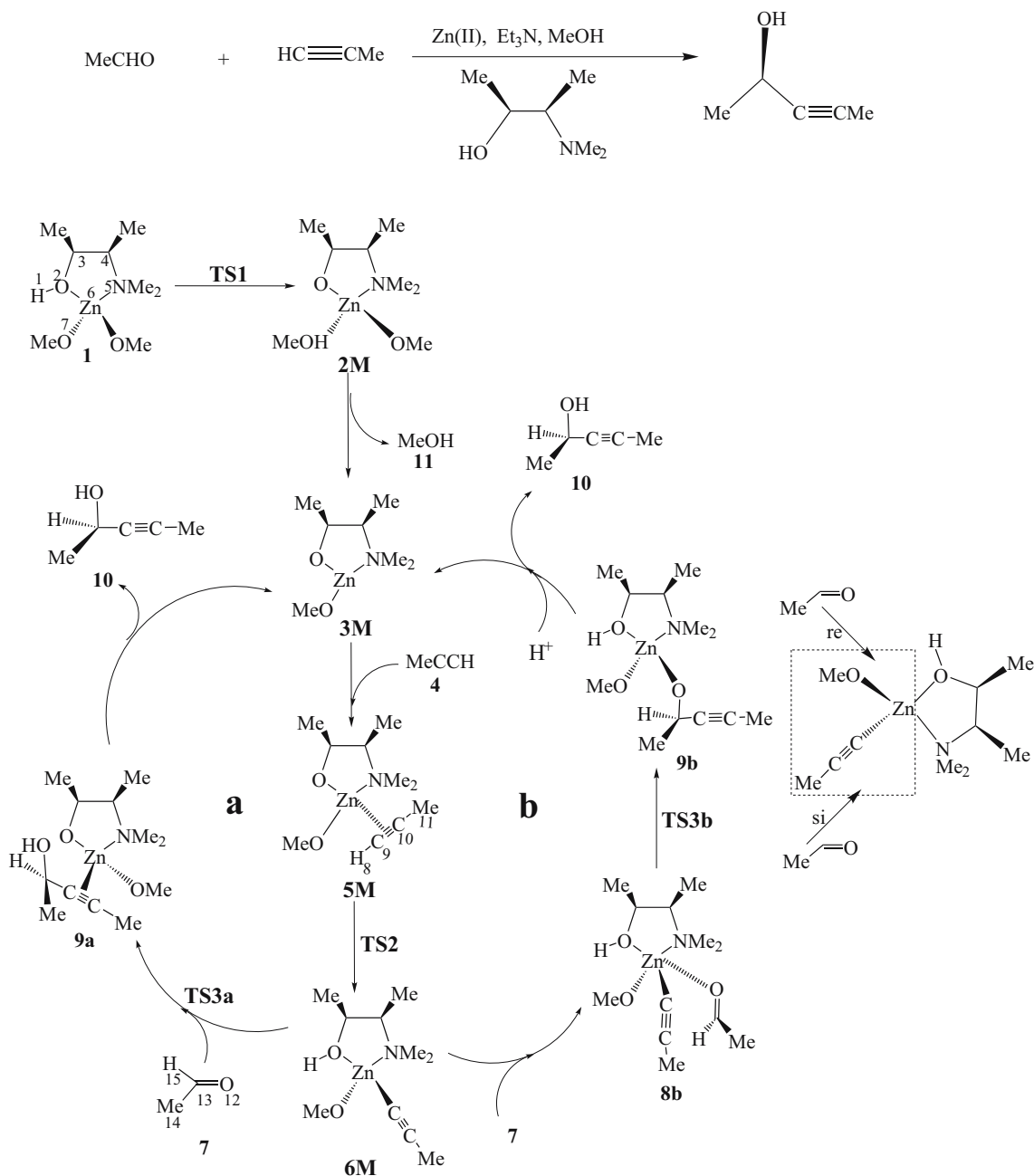


Fig. 1 The enantioselective alkynylation of aldehyde catalyzed by chiral Zinc(II)-complexes

shown in Fig. 2. To obtain more exact energies, single-point energy calculations at the B3LYP/6-31+G(d,p) level were carried out on the B3LYP/6-31G(d,p) geometries. All the computations were carried out with the Gaussian 03 program package [28]. In addition, the electron densities at the bond-critical points (BCP) and the ring-critical points (RCP) for some species were calculated using the AIM2000 program [29]. Total electronic energies corrected with zero-point energies, E , formation energies, ΔE , reaction energy barriers, ΔE^\ddagger , and the first two vibrational frequencies, ν_1 and ν_2 , are summarized in Table 1. In all figures of the optimized structures, only some important atoms and bonds are presented for clarity.

Results and discussion

Formation of the active catalyst **3M**

The optimized structure of the catalyst **1** is shown in Fig. 3. The H(1)–O(2) bond is 0.998 Å. The catalyst is of anamorphic tetrahedral structure and the O(2)–N(5)–Zn(6)–O(7) torsion angle is 120.5°.

The transfer of H(1) from O(2) to O(7) in the catalyst **1** leads, via the transition states TS1 and TS1', to the intermediates **2M** and **2M'**. In the transition states TS1 and TS1', the H(1)–O(2) bonds lengthen considerably and the H(1)–O(7) bonds are shortened compared with those in the

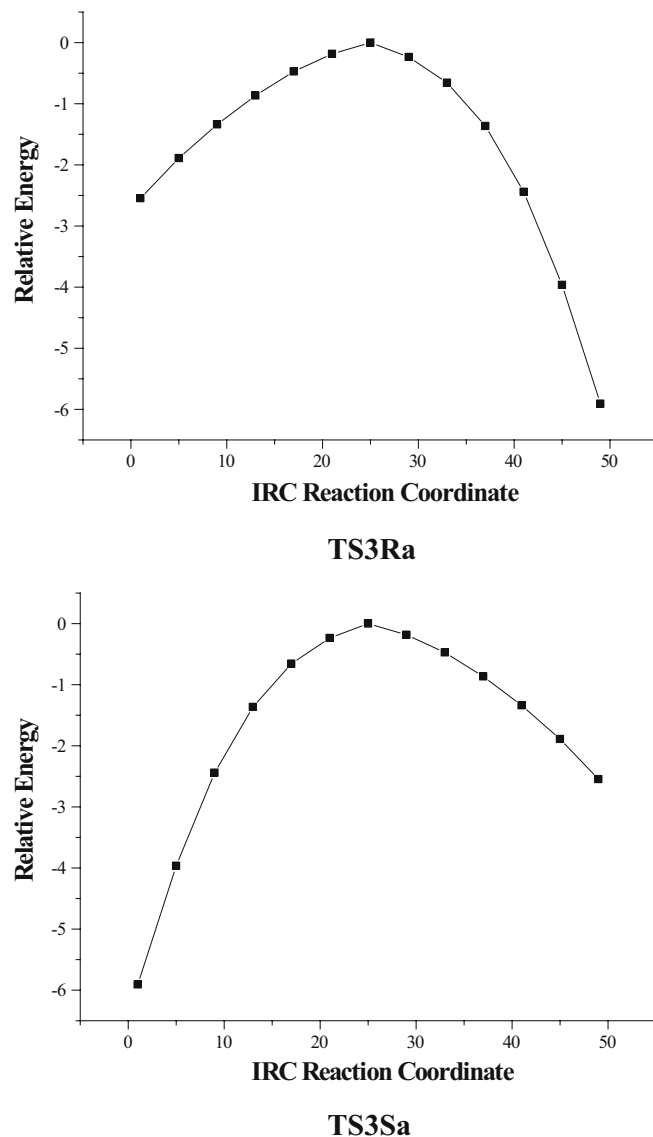


Fig. 2 The IRC calculations on some transition states

catalyst 1. It is clear that there is a significant interaction between H(1) and O(7), and the H(1)–O(2) bonds are weakened greatly. As illustrated in Fig. 4, there is a H(1)–O(2)–Zn–O(7) four-membered ring for each of these transition states and the electron densities of their RCPs are 0.0402 and 0.0405, respectively. The present computations show that the fracture of the H(1)–O(2) bonds and the formation of the H(1)–O(7) bonds may be in concurrence. The complexes 2M and 2M' are similar to catalyst 1 in structure and all have anamorphic tetrahedral structures. In the complexes 2M and 2M', Zn–O(2) is a σ -bond and Zn–O(7) is a σ -coordinate covalent bond, whereas Zn–O(2) in the catalyst is a σ -coordinate covalent bond and Zn–O(7) is a σ -bond. The decomposition of methanol from 2M and 2M' generates the active catalyst 3M. The ZnL₃ complex

3M is almost planar and the O(2)–N(5)–Zn(6)–O(7) torsion angle is 173.9°.

Formation of the catalyst-alkynyl complexes 6M and 6M'

The reaction of the terminal alkyne 4 with the active catalyst 3M leads to the catalyst-alkyne complexes 5M and 5M'. The transfer of H(8) to O(2) in 5M and 5M' traverses the transition states TS2 and TS2', respectively, and then leads to the catalyst-alkynyl complexes 6M and 6M'. As illustrated in the NBO analysis, 5M and 5M' exhibit π -back bonding. The occupied π -orbital of alkyne acts on the empty incoordinate sp³-hybrid orbital of zinc leading to the σ -coordinate bond and, on the other hand, the occupied d-orbital (d_{xy}, d_{xz}, d_{yz}) of zinc acts on the empty π^* orbital of the alkyne, leading to π -back bonding. Obviously, the formation of the π -bonds lowers the system energies and makes the complexes 5M and 5M' more stable. Compared with H(8)–C(9) of 4, the H(8)–C(9) bonds of 5M and 5M' are weakened (bond: 1.064→1.069 Å the electron density of the BCP: 0.2891→0.2872). The transition states TS2 and TS2' are similar to the transition states TS1 and TS1' in geometric structure. In the transition states TS2 and TS2', the σ – π coordinate bonds between alkyne and zinc are fractured and the H(8)–O(2) distances become shorter and the H(8)–C(9) bonds become longer, which implies a strong interaction between H(8) and O(2) and the H(8)–C(9) bonds are weakened remarkably. As shown in Fig. 4, each of these transition states involves a H(8)–O(2)–Zn–C(9) four-membered ring and the electron densities of the RCPs are 0.0411 and 0.0306, respectively. The present computations show that the fracture of the H(8)–O(2) bonds and the formation of the H(8)–C(9) bonds may be in concurrence. 6M and 6M' are similar to the catalyst in structure. As shown by the NBO analysis, the Zn–C(9) bonds of 6M and 6M' are strong single bonds and the natural bond orbital energies of these σ bonds are -1185.75 and -1196.20 kJ mol⁻¹, respectively.

In addition, we tried to compute the direct coordination of alkyne to the catalyst 1, the transfer of H(8) in alkyne to O(7) in the catalyst, and the decomposition of methanol leading to the catalyst-alkynyl complexes 6M and 6M', but all of our efforts failed.

The reaction mode “a”

The reaction mode “a” expresses the attack of aldehyde on the *re*-surface of the complexes 6M and 6M' (Fig. 1). The attack of aldehyde leads to the formation of the catalyst-ethanol complexes 9Ra, 9Sa, 9Ra', and 9Sa', and the corresponding transition states are TS3Ra, TS3Sa, TS3Ra', and TS3Sa'. As shown in Figs. 4 and 5, there are strong interactions between H(8) and O(12) and between C(9) and C(13) in these transition states. The transition states

Table 1 Total energies $E(\times 2625.5 \text{ kJ mol}^{-1})$, formation energies $\Delta E(\text{kJ mol}^{-1})$, reaction energy barriers $\Delta E^\#(\text{kJ mol}^{-1})$, and frequencies (cm^{-1}) for all the compounds

	ZPE	$E6-31G(d,p)$ a	$\geq Ea$	$\geq E?a$	$v1$	$v2$	$E6-31+G(d,p)$ b	$\geq Eb$	$\geq E\#b$
1	0.2966	-2,376.8124			39.9	61.1	-2,377.1664		
TS1	0.2923	-2,376.8101		6.04	834.21i	32.14	-2,377.1576		23.10
TS1'	0.2919	-2,376.8114		2.63	762.93i	25.51	-2,377.1586		20.48
2M	0.2964	-2,376.8140	-4.20		33.69	45.00	-2,377.1665	-0.26	
2M'	0.2959	-2,376.8134	-2.63		25.44	42.98	-2,377.1656	2.10	
3M	0.2423	-2,261.1155			25.28	46.54	-2,261.4165		
4	0.0556	-116.6038			348.2	348.2	-116.6672		
5M	0.2996	-2,377.7326	-34.92		30.62	36.54	-2,378.0879	-11.03	
5M'	0.2992	-2,377.7321	-33.61		21.08	41.71	-2,378.0878	-10.76	
TS2	0.2962	-2,377.7110		56.71	1,184.54i	28.50	-2,378.0611		70.36
TS2'	0.2961	-2,377.7133		49.36	1,070.23i	28.13	-2,378.0635		63.80
6M	0.3020	-2,377.7361	-9.19		17.0	20.8	-2,378.0948	-18.12	
6M'	0.3021	-2,377.7377	-14.70		33.6	37.2	-2,378.0958	-21.00	
7	0.0556	-153.7801			155.9	505.1	-153.8452		
8Rb	0.3587	-2,531.5263	-26.52		13.8	23.4	-2,531.9464	-14.18	
8Sb	0.3591	-2,531.5235	-19.17		14.8	32.1	-2,531.9425	-3.94	
8Rb'	0.3592	-2,531.5295	-30.72		21.4	31.8	-2,531.9472	-16.28	
8Sb'	0.3590	-2,531.5279	-26.52		24.5	30.3	-2,531.9465	-14.44	
TS3Ra	0.3584	-2,531.5096		17.33	387.0i	22.5	-2,531.9246		43.06
TS3Sa	0.3579	-2,531.5046		30.46	386.7i	13.9	-2,531.9206		53.56
TS3Ra'	0.3579	-2,531.5081		25.47	406.2i	22.6	-2,531.9238		45.16
TS3Sa'	0.3581	-2,531.5061		30.72	384.9i	24.4	-2,531.9220		49.88
TS3Rb	0.3593	-2,531.4883		99.77	380.2i	23.7	-2,531.9031		113.68
TS3Sb	0.3594	-2,531.4878		93.73	383.4i	22.8	-2,531.9025		105.02
TS3Rb'	0.3595	-2,531.4934		94.78	384.4i	19.5	-2,531.9081		102.66
TS3Sb'	0.3592	-2,531.4937		89.79	381.8i	20.8	-2,531.9082		100.56
9Ra	0.3629	-2,531.5364	-53.04		22.7	41.7	-2,531.9586	-46.21	
9Sa	0.3627	-2,531.5381	-57.50		24.3	38.9	-2,531.9607	-51.72	
9Ra'	0.3624	-2,531.5389	-55.40		18.8	35.7	-2,531.9615	-53.82	
9Sa'	0.3624	-2,531.5377	-52.25		18.1	44.4	-2,531.9596	-48.83	

TS3Ra, TS3Sa, TS3Ra', and TS3Sa' involve a H(8)–O(2)–Zn–C(9)–C(13)–O(12) six-membered ring and the electron densities of the RCPs are 0.0112, 0.0107, 0.0112, and 0.0109, respectively. Compared with those in the catalyst–alkynyl complexes 6M and 6M', the H(8)–O(2) and O(12)–C(13) bonds in these transition states are weakened greatly and are lengthened by about 0.12 and 0.08 Å, and the electron densities of their BCPs are decreased by about 0.11 and 0.055. It is clear that the weakening of the H(8)–O(2) and O(12)–C(13) bonds is of advantage for the transfer of H(8) to O(12). As shown, the formation of the H(8)–O(12) and C(9)–C(13) bonds and the fracture of the H(8)–O(2) bonds may be in concurrence.

The decomposition of the catalyst–ethanol complexes 9Ra, 9Sa, 9Ra', and 9Sa' results in the products 10 and leads to the regeneration of the active catalyst 3M. As illustrated in the NBO analysis, the complexes 9Ra, 9Sa, 9Ra', and 9Sa' also include σ – π coordinate bonds. As shown in Fig. 5, there are hydrogen bonds between H(8) and O(2), the distances of which are, respectively, 1.709,

1.685, 1.670, and 1.682 Å. It is these hydrogen bonds that lead to the ring structures in these complexes. In addition, the O(12)–C(13) π bonds (the carbonyl π bonds) in these complexes are broken.

The reaction mode “b”

The reaction mode “b” expresses the attack of aldehyde on the *si*-surface of 6M and 6M'. The addition of aldehyde to the complexes 6M and 6M' leads to the catalyst–alkynyl–aldehyde complexes 8Rb, 8Sb, 8Rb', and 8Sb', and then generates the catalyst–ethanol complexes 9Rb, 9Sb, 9Rb', and 9Sb' via the transition states TS3Rb, TS3Sb, TS3Rb', and TS3Sb'. In the complexes 8Rb, 8Sb, 8Rb', and 8Sb' with ZnL₅ coordination, the distances between C(9) and C(13) are 4.074, 3.316, 3.840, and 3.273 Å, respectively, and the carbonyl of aldehyde is weakened (the electron density of its BCP is decreased by about 0.01). In the transition states TS3Rb, TS3Sb, TS3Rb', and TS3Sb', the C(9)–C(13)

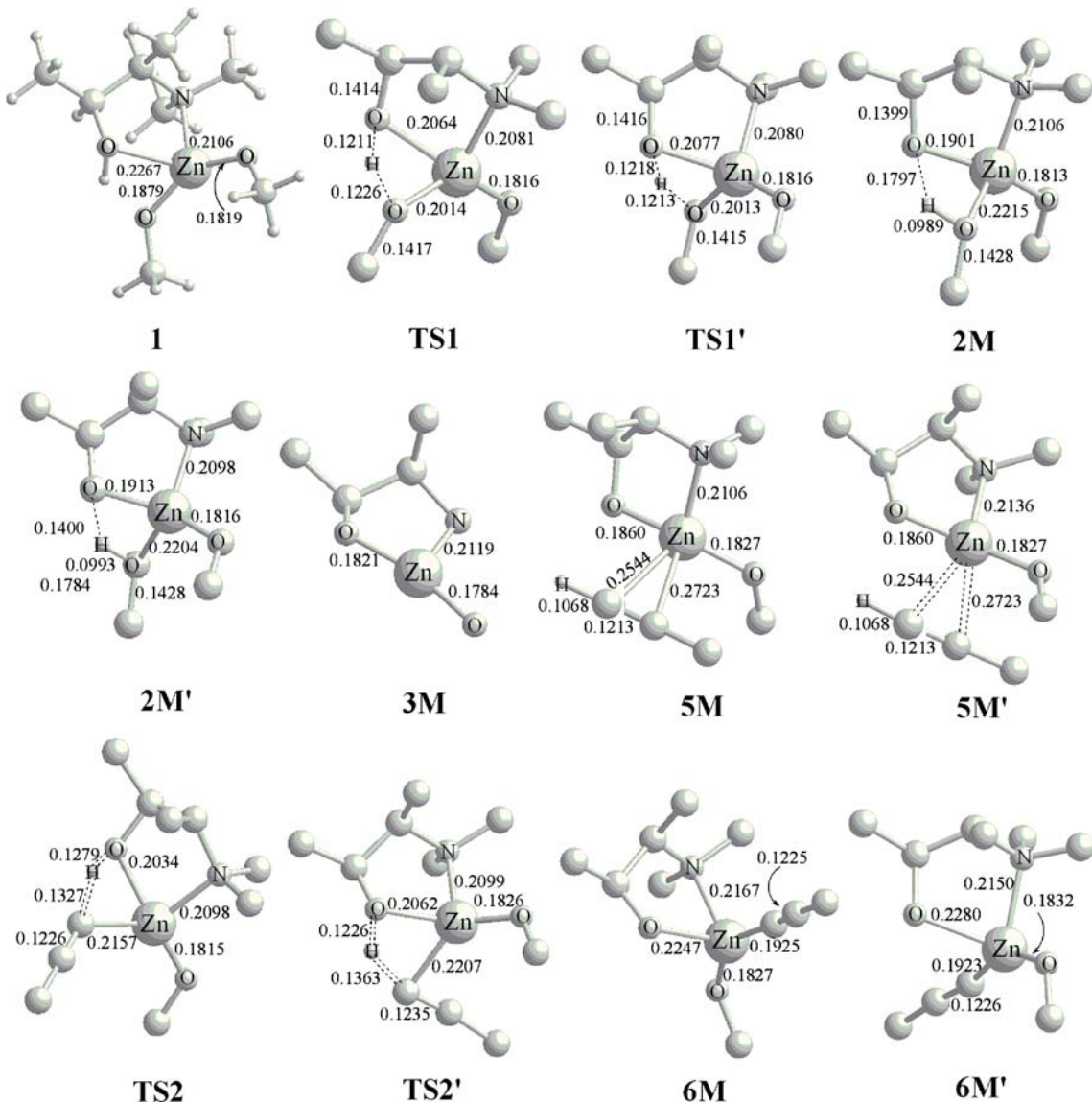


Fig. 3 The optimized geometries of the catalyst and some intermediate states

distances are shortened considerably and the O(12)–C(13) bonds are lengthened greatly. These results imply that there is a significant interaction between C(9) and C(13) and the O(12)–C(13) bonds are weakened greatly. As shown in Fig. 4, there is a C(9)–Zn–O(12)–C(13) four-membered ring for each of these transition states and the electron densities of the RCPs are 0.0318, 0.0322, 0.0299, and 0.0299, respectively. In addition, the electron densities of the BCPs for the Zn–C(9) bonds in the transition states are decreased by about 0.04 relative to those of the complexes 8, and thus these bonds are weakened. The fracture of the Zn–C(9) bonds and the formation of the C(9)–C(13) bonds may also be in concurrence. Unlike the complexes 9Ra, 9Sa, 9Ra', and 9Sa', the complexes 9Rb, 9Sb, 9Rb', and 9Sb' do not involve any ring structures, because there are no hydrogen

bonds in the complexes, and the carbonyl π -bonds are broken. The decomposition of the complexes 9 also results in the products 10.

Overview of the mechanism

By investigating the structures of all the intermediates and transition states, it is known that the intermediates and transition states marked by “R” lead to the (*R*)-ethanol and those marked by “S” result in the (*S*)-ethanol. As demonstrated in Fig. 1, there are two chiral carbon atoms in catalyst 1 and their chirality remains unchanged in the reaction. The enantioselective alkynylation of aldehyde can cause the carbonyl carbon of aldehyde to become the third

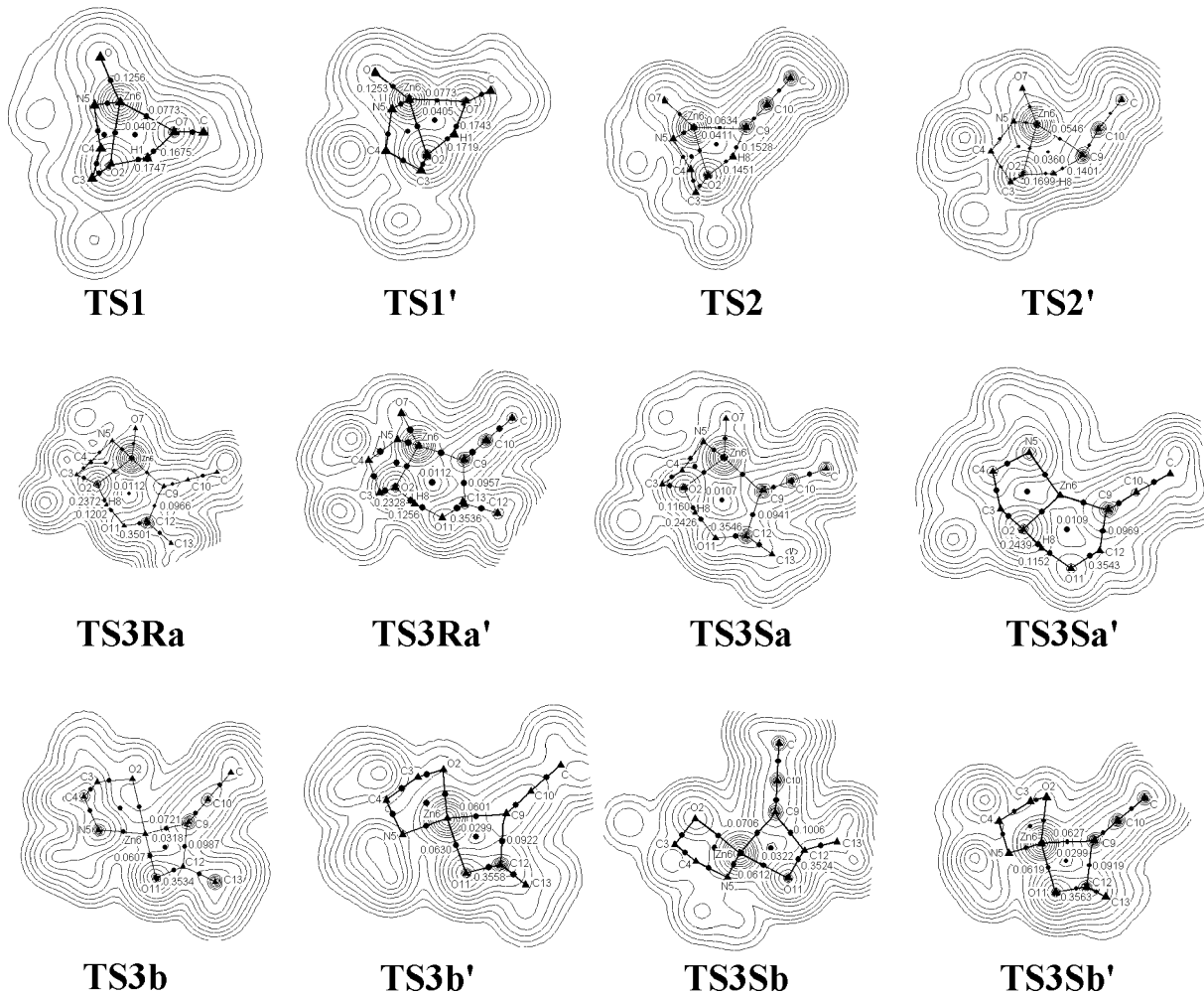


Fig. 4 The two-dimensional electron density contours for all the transition states (including electron densities of some selected BCPs and RCPs)

chiral carbon, that is of (*R*)- or (*S*)-chirality. Therefore, the intermediates and transition states marked by “R” or “S”, such as 8Rb and 8Sb, 9Rb and 9Sb, TS3Ra, TS3Sa, TS3Rb and TS3Sb, etc., are diastereoisomers and have different energies. Fig. 6 illustrates the DFT energy relationship for the asymmetric alkynylation of aldehyde.

Figure 1 and Table 1 show that the formation of the complexes 2M, 2M', and 3M is endothermic. Because of the π -back bonding between the terminal alkyne and zinc in the catalyst-alkyne complexes 5M and 5M', these two complexes are stable and thus their formation is exothermic. The strong single Zn–C(9) bonds of the catalyst-alkynyl complexes 6M and 6M' lower the system energies a little and thus the formation of 6M and 6M' is exothermic. For the reaction mode “a”, there are σ – π coordinate covalent bonds and the H(8)–O(2) hydrogen bonds in the catalyst-ethanol complexes 9Ra, 9Sa, 9Ra' and 9Sa', and thus the formation of these catalyst-ethanol complexes is also exothermic. For the reaction mode “b”,

prior to the formation of the catalyst–ethanol complexes, the catalyst–alkynyl–aldehyde complexes 8Rb, 8Sb, 8Rb', and 8Sb' are generated. Due to the formation of the stable Zn–O(12) bonds, the formation of the catalyst–alkynyl–aldehyde complexes 8 is exothermic. The formation of the catalyst–ethanol coordination 9Rb, 9Sb, 9Rb', and 9Sb' is also exothermic. In addition, as illustrated in Table 1 and Fig. 6, this enantioselective alkynylation of aldehyde is endothermic and the total absorbed energy is about 31 kJ mol⁻¹.

In the transition states TS2 and TS2', the σ – π coordinate bonds between zinc and alkyne are broken and there are strained four-membered rings. The energies for these transition states are high. The transition states TS3Ra, TS3Sa, TS3Ra', and TS3Sa' have stable six-membered rings and this reaction step is related to the fracture of the H(8)–O(2), Zn–C(9), and O(12)–C(13) π -bonds and the formation of the H(8)–O(12), C(9)–C(13), and the zinc–alkyne σ – π coordinate bonds. The transition states TS3Rb, TS3Sb,

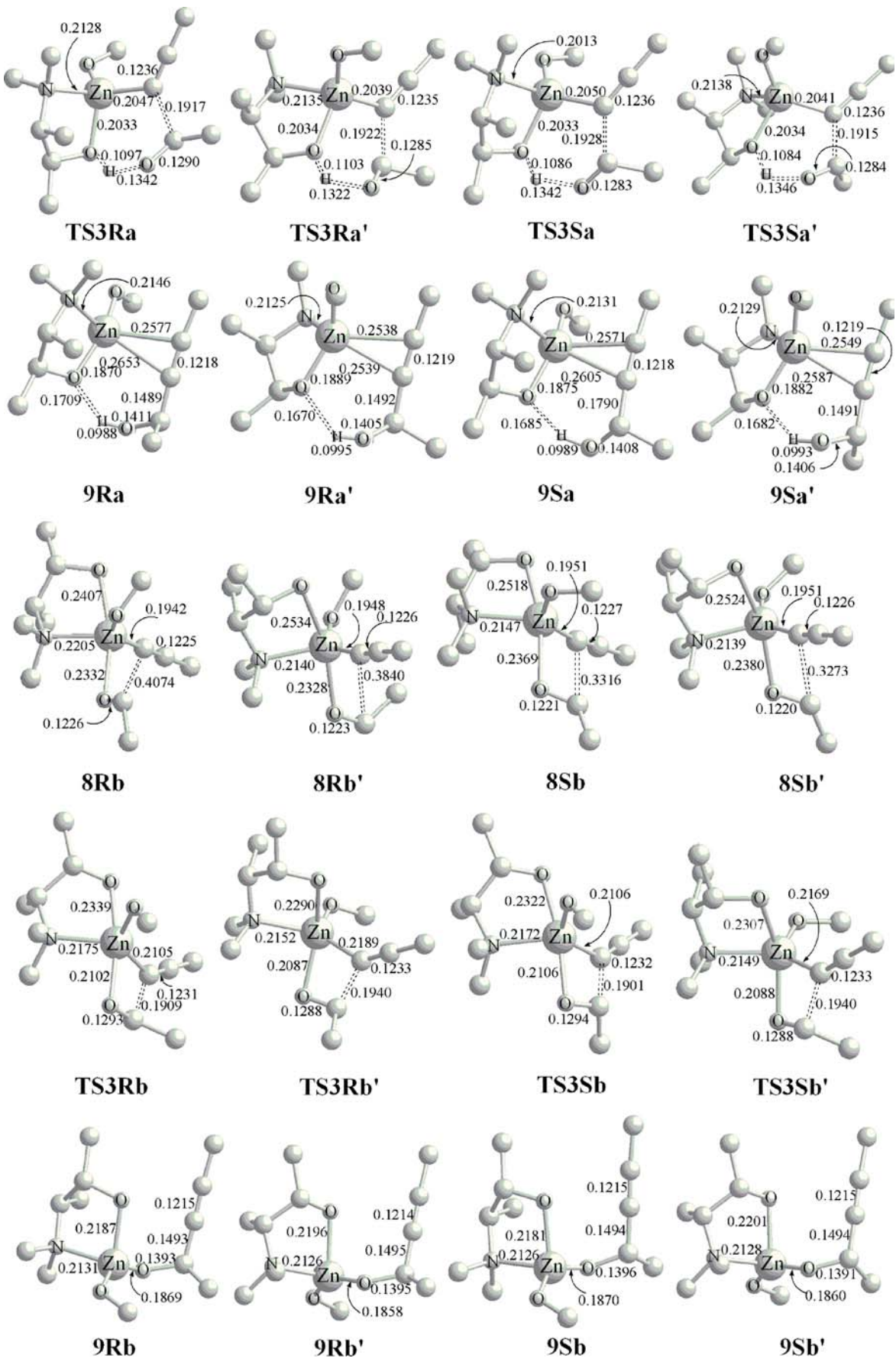
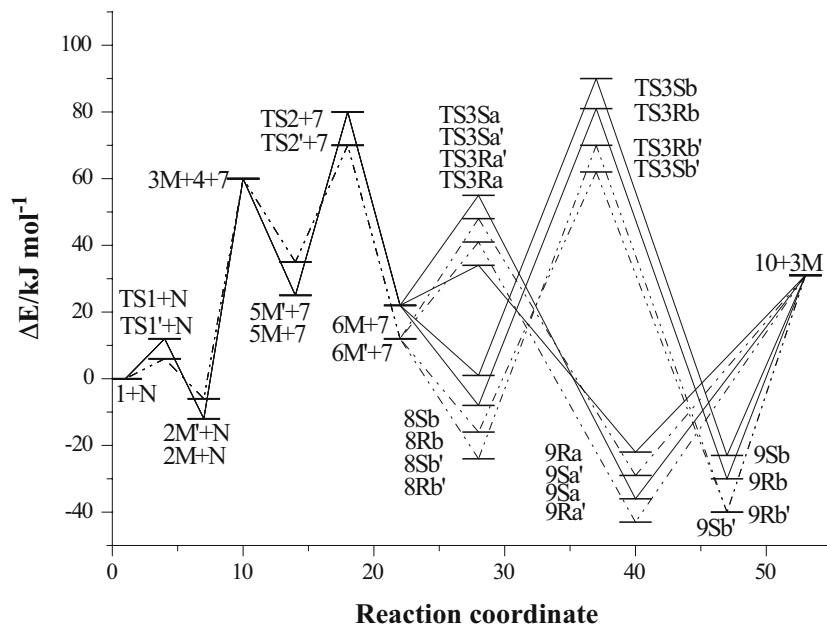


Fig. 5 The optimized geometries of the reaction modes "a" and "b"

Fig. 6 Energy relationship for the enantioselective alkynylation of aldehyde



TS3Rb', and TS3Sb' have strained four-membered rings and the corresponding reaction step is related to the fracture of the Zn–C(9) and O(12)–C(13) π -bonds and the formation of the C(9)–C(13) bonds. The bonds formed in the transition states for the reaction mode “a” are stronger than those in the transition states for the reaction mode “b” by roughly one zinc-alkyne σ – π coordinate bond. On the other hand, the strain for the four-membered ring is greater than that for the six-membered ring, and thus the six-membered ring is more stable than the four-membered ring. Therefore, the energies of the transition states TS3Ra, TS3Sa, TS3Ra', and TS3Sa' are lower than those of the transition states TS3Rb, TS3Sb, TS3Rb', and TS3Sb'. Table 1 shows that the energies of the transition states for the reaction mode “a” are lower than those of the transition states for the reaction mode “b” by 32–58 kJ mol^{−1}. The energy barriers of the transition states TS3Ra, TS3Sa, TS3Ra', and TS3Sa' are lower than those of the transition states TS3Rb, TS3Sb, TS3Rb', and TS3Sb' by 47–60 kJ mol^{−1}.

As discussed above, both the reaction mode “a” and the reaction mode “b” have four reaction channels. The energy barriers of the transition states for the mode “a” are lower than those of the transition states for the mode “b”. Both reaction modes pass through the transition states TS2 and TS2' with a high energy. Therefore, the enantioselective alkynylation of aldehyde catalyzed by chiral zinc(II)-complexes mainly pass through the reaction mode “a”. The energy barriers of the transition states TS3Ra, TS3Sa, TS3Ra', and TS3Sa' are 43.06, 53.56, 45.16 and 49.88 kJ mol^{−1}, respectively. It is clear that the reaction channel 1→TS1→2M→3M→5MTS2→6M→TS3Ra→9Ra→10R

is the dominant channel leading to the chiral ethanol. The dominant products obtained from this reaction channel are of (*R*)-chirality, in good agreement with experiment [8, 10, 13]. Furthermore, the energy barriers of TS2 are much higher than the barrier of TS3Ra in the reaction mode “a”. The rate-determining step for the enantioselective alkynylation of aldehyde catalyzed by the chiral zinc(II)-complexes is therefore the formation of the catalyst–alkynyl complexes 6M, and the formation of the catalyst–ethanol complexes 9 is the chirality-determining step for this alkynylation reaction.

Conclusion

In summary, the enantioselective alkynylation of aldehyde catalyzed by chiral zinc(II)-complexes involves eight possible reaction channels. The alkynylation of aldehyde goes mainly through the formation of the catalyst–alkyne complexes, the catalyst–alkynyl complexes, and the catalyst–ethanol complexes. The formation of the catalyst–ethanol complexes is the chirality-determining step for the alkynylation. The transition state for the chirality-determining step has a six-membered ring. The alkynylation reaction is endothermic. The dominant products predicted theoretically are of (*R*)-chirality, in good agreement with experiment.

Acknowledgement This work was supported by the key project of science and technology of the ministry of education, People's Republic of China (NO.104263).

References

1. Pu L, Yu HB (2001) *Chem Rev* 101:757–824
2. Frantz DE, Fässler R, Carreira EM (1999) *J Am Chem Soc* 121:11245–11246
3. Jiang B, Si YG (2004) *Angew Chem Int Ed* 43:216–218
4. Yang XW, Shen JH, Da CS, Wang HS, Su W, Wang R, Chan ASC (2000) *J Org Chem* 65:295–296
5. Xu ZQ, Wang R, Xu JK, Da CS, Yan WJ, Chen C (2003) *Angew Chem Int Ed* 42:5747–5749
6. Da CS, Han ZJ, Ni M, Yang F, Liu DX, Zhou YF (2003) *Tetrahedron: Asymmetry* 14:659–665
7. Tombo GMR, Didier E, Loubinoux B (1990) *Synlett* 547–548
8. Frantz DE, Fässler R, Carreira EM (2000) *J Am Chem Soc* 122:1806–1867
9. Boyall D, López F, Sasaki H, Frantz DE, Carreira EM (2000) *Org Lett* 2:4233–4236
10. Frantz DE, Fässler R, Tomooka CS, Carreira EM (2000) *Acc Chem Res* 33:373–381
11. Sasaki H, Boyall D, Carreira EM (2001) *Helv Chim Acta* 84:964–971
12. Bode JW, Carreira EM (2001) *J Am Chem Soc* 123:3611–3612
13. Anand NK, Carreira EM (2001) *J Am Chem Soc* 123:9687–9688
14. Fischer C, Carreira EM (2001) *Org Lett* 3:4319–4321
15. Fässler R, Frantz DE, Oetiker J, Carreira EM (2002) *Angew Chem Int Ed* 41:3054–3056
16. Wei C, Li CJ (2002) *J Am Chem Soc* 124:5638–5639
17. Li M, Zhu XZ, Yuan K, Cao BX, Hou XL (2004) *Tetrahedron: asymmetry* 15:219–222
18. Zhou YF, Wang R, Xu XQ, Yan WJ, Liu L, Gao YF, Da CS (2004) *Tetrahedron: asymmetry* 15:589–591
19. Tan L, Chen CY, Tillyer RD, Grabowski EJJ, Reider PJ (1999) *Angew Chem Int Ed* 38:711–713
20. Kitamura M, Okada S, Suga S, Noyori R (1989) *J Am Chem Soc* 111:4028–4036
21. Kitamura M, Okada S, Niwa M, Noyori R, Zhai Z, Suga S (1994) *J Phys Chem* 98:12776–12781
22. Yamakawa M, Noyori R (1995) *J Am Chem Soc* 117:6327–6335
23. Yamakawa M, Noyori R (1999) *Organometallics* 18:128–133
24. Zhang HL, Jiang F, Zhang XM, Cui X, Gong LZ, Mi AQ, Jiang YZ, Wu YD (2004) *Chem Eur J* 10:1481–1492
25. Kitamura M, Yamakawa M, Oka H, Suga S, Noyori R (1996) *Chem Eur J* 2:1173–1181
26. Flükiger P, Lüthi HP, Portmann S, Weber J (2000–2002) MOLEKEL 4.3. Swiss Center for Scientific Computing, Manno, Switzerland
27. Portmann S, Lüthi HP (2000) *CHIMIA* 54:766–770
28. Frisch MJ, Trucks GW, Schlegel HB, Scuseria GE, Robb MA, Cheeseman JR, Montgomery JA, Vreven Jr T, Kudin KN, Burant JC, Millam JM, Iyengar SS, Tomasi J, Barone V, Mennucci B, Cossi M, Scalmani G, Rega N, Petersson GA, Nakatsuji H, Hada M, Ehara M, Toyota K, Fukuda R, Hasegawa J, Ishida M, Nakajima T, Honda Y, Kitao O, Nakai H, Klene M, Li X, Knox JE, Hratchian HP, Cross JB, Adamo C, Jaramillo J, Gomperts R, Stratmann RE, Yazyev O, Austin AJ, Cammi R, Pomelli C, Ochterski JW, Ayala PY, Morokuma K, Voth GA, Salvador P, Dannenberg JJ, Zakrzewski VG, Dapprich S, Daniels AD, Strain MC, Farkas O, Malick DK, Rabuck AD, Raghavachari K, Foresman JB, Ortiz JV, Cui Q, Baboul AG, Clifford S, Cioslowski J, Stefanov BB, Liu G, Liashenko A, Piskorz P, Komaromi I, Martin RL, Fox DJ, Keith T, Al-Laham MA, Peng CY, Nanayakkara A, Challacombe M, Gill PMW, Johnson B, Chen W, Wong MW, Gonzalez C, Pople JA (2003) Gaussian 03, Revision B.03. Gaussian Inc, Pittsburgh PA
29. Biegler-König F, Schönbohm J, Derdau R, Bayles D, Bader RFW (2000) AIM 2000, Version 1